Geochemistry, Geophysics, Geosystems

RESEARCH ARTICLE
10.1029/2020GC009375

Segment-Scale Seismicity of the Ultraslow Spreading Knipovich Ridge

Michaela Meier[1], Vera Schlindwein[1], John-Robert Scholz[1], Jonah Geils[1,2], Mechita C. Schmidt-Aursch[1], Frank Krüger[3], Wojciech Czuba[4], and Tomasz Janik[4]

[1]Alfred Wegener Institute, Helmholtz Centre for Polar and Marine Research, Bremerhaven, Germany, [2]Faculty of Geosciences, University of Bremen, Bremen, Germany, [3]Institute for Geosciences, University of Potsdam, Potsdam, Germany, [4]Institute of Geophysics, Polish Academy of Sciences, Warszawa, Poland

Key Points:

- Magma-poor sections are distinguished from magma-rich sections by deeper hypocenters and an absence of shallow seismicity
- Shallowing maximum earthquake depths over distances of 70 km suggest along-axis melt focusing toward major volcanic centers
- Major detachment faults on the highly oblique spreading Knipovich Ridge were not obvious in the observed seismicity

Supporting Information:

- Supporting Information S1
- Figure S1
- Figure S2
- Figure S3
- Figure S4
- Figure S5
- Figure S6
- Table S1

Correspondence to:
M. Meier,
michaela.meier@awi.de

Citation:
Meier, M., Schlindwein, V., Scholz, J.R., Geils, J., Schmidt-Aursch, M. C., Krüger, F., et al. (2021). Segment-scale seismicity of the ultraslow spreading Knipovich Ridge. *Geochemistry, Geophysics, Geosystems*, *22*, e2020GC009375. https://doi.org/10.1029/2020GC009375

Received 12 AUG 2020
Accepted 30 OCT 2020

Abstract Ultraslow spreading ridges form the slowest divergent plate boundaries and exhibit distinct spreading processes in volcanically active magmatic sections and intervening amagmatic sections. Local seismicity studies of ultraslow spreading ridges until now cover only parts of segments and give insight into spreading processes at confined locations. Here, we present a microseismicity data set that allows to study spreading processes on the scale of entire segments. Our network of 26 ocean bottom seismometers covered around 160 km along axis of the ultraslow spreading Knipovich Ridge in the Greenland Sea and recorded earthquakes for a period of about 1 year. We find seismicity varying distinctly along-axis. The maximum earthquake depths shallow over distances of 70 km toward the Logachev volcanic center. Here, swarm activity occurs in an otherwise aseismic zone. Melts may thus be guided along the subparallel topography of the lithosphere-asthenosphere boundary toward major volcanic centers explaining the uneven along-axis melt distribution typical for ultraslow ridges. Absence of shallow seismicity in the upper 8 km of the lithosphere with a band of deep seismicity underneath offsets presumably melt-poor regions from magma richer sections. Aseismic deformation in these regions may indicate weakening of mantle rocks by alteration. We do not find obvious indications for major detachment faulting that characterizes magma-poor spreading at some ultraslow spreading segments. The highly oblique spreading of Knipovich Ridge may be the reason for a fine-scale segmentation of the seismic activity with zones of weak seismicity possibly indicating transform motion on short obliquely oriented faults.

Plain Language Summary At mid-ocean spreading ridges, tectonic plates drift apart and new seafloor is built by upwelling magma. The slowest spreading ridges do not receive enough magma to build new seafloor along the entire ridge. Rather, they show widely spaced volcanic centers with magma-poor areas in-between. The study of small earthquakes with seismometers placed on the seafloor has greatly helped to understand how new seafloor forms. Since such studies require substantial logistic effort, only confined ridge sections have been studied and spreading processes operating at segment-scale remain poorly understood. In this study, we present for the first time observations of earthquakes covering several segments and one major volcanic center along the Knipovich Ridge in the Greenland Sea. Underneath the volcano, earthquake swarms and a gap in seismicity indicate recent magmatic activity. The maximum depth of earthquakes marks the thickness of the mechanically strong lithosphere. It shallows over 70 km toward the volcano such that melts can be channeled over large distances to the prominent volcanoes. Magma-poor regions have deep earthquakes but do not show earthquake activity in the upper 8 km. We suppose that water reacts with the mantle rocks that become too weak to break in earthquakes.

1. Introduction

Ultraslow spreading ridges have become an important study area for the interplay of magmatism and tectonics in spreading processes. Widely spaced volcanic centers receive more melt than the ridge on average does (Cannat et al., 2003; Standish et al., 2008), while amagmatic segments in between receive less melt and exhibit mantle rocks at the seafloor (Michael et al., 2003). The underlying proposed mechanism of melt focusing (Sauter & Cannat, 2010) describes melt traveling along the lithosphere-asthenosphere boundary (LAB) from amagmatic segments toward volcanic centers at magmatic segments (Cannat et al., 2003; Montési et al., 2011). Undulations of the LAB seen as hint on melt focusing have been mapped by local seismicity (Schlindwein & Schmid, 2016). Volcanic centers with their high melt supply can feed subordinate

volcanoes (Sauter et al., 2001), which is observed at the Segment 8 volcano along the Southwest Indian Ridge (SWIR; Meier & Schlindwein, 2018; Schmid et al., 2017). The basaltic seafloor at magmatic segments is often referred to as rough, while the seafloor along amagmatic sections with exposed mantle rocks is smooth (Cannat et al., 2008; Okino et al., 2002). The mantle rocks at the seafloor allow serpentinization, which significantly reduces the lithospheric strength (Escartin et al., 2001) and supposedly builds aseismic zones in the upper lithosphere (Schlindwein & Schmid, 2016). The considerable influence of serpentinization becomes obvious in lithospheric strength profiles of amagmatic segments (Cannat et al., 2019). Along amagmatic segments spreading cannot be accommodated by magmatism, it is mainly hosted by detachment faulting (Cannat et al., 2019; Reston & McDermott, 2011; Sauter et al., 2013). This can be visible as an asymmetric distribution of teleseismicity. The resulting stripe and gap pattern shows enhanced seismicity in asymmetric ridge sections (Escartin et al., 2008; Simão et al., 2010). Local seismicity of detachments is observed as hypocenters aligning along dipping planes (deMartin et al., 2007; Tao et al., 2020; Yu et al., 2018) or following the stress regime (Parnell-Turner et al., 2017).

The dimensions of local ocean bottom seismometer (OBS) networks that greatly helped to shed light on active spreading processes at mid-ocean ridges have often been limited to one segment or one specific feature (e.g., Schlindwein & Schmid, 2016; Tao et al., 2020) such that questions about the connection of segments and spreading processes on larger scales remain poorly understood. The term "segment" is not clearly defined for ultraslow spreading ridges, since transform faults as the common first-order segment boundaries are very rare or completely absent as along the Knipovich Ridge (Kokhan et al., 2012). The complex bathymetry complicates recognizing nontransform discontinuities to clearly define segment boundaries. The Gakkel Ridge for example is split into three extended "zones" based on bathymetry and petrology (Michael et al., 2003), while the SWIR is split into significantly shorter segments mainly according to bathymetry, magnetic and gravity data (Cannat et al., 2003) and each typically hosting a volcanic center, some of them only subordinate. In this study, we refer to "segment" as the area around one major volcanic center. For our segment-scale OBS study we deployed instruments covering two major volcanic centers as defined in Curewitz et al. (2010). The (sub-) segmentation we infer is based on seismological data.

OBS networks resolve earthquake hypocenter locations within few kilometers and are used to study detachments (e.g., Parnell-Turner et al., 2017; Tao et al., 2020), dike injections (Meier & Schlindwein, 2018), lithospheric structure (Schmid & Schlindwein, 2016), and variations in lithospheric thickness (Schlindwein & Schmid, 2016). Teleseismic or hydroacoustic data have been used to study active spreading processes at segment-scale (e.g., Escartin et al., 2008; Simão et al., 2010; Smith et al., 2003). However, these data cannot resolve earthquake depths and epicentral location uncertainties are typically larger than 10 km. Segment-scale OBS networks are needed to investigate processes in detail and gain insights into large-scale melt focusing and segmentation, the appearance of detachment faults, transfer regions and the sub-segmentation of segments. To find answers to these questions, we deployed an extensive OBS network of more than 160 km along-axis extent along the Knipovich Ridge covering a major volcanic center and areas lacking signs of magmatism. The Knipovich Ridge was chosen despite its geoscientific complexities (following paragraph), because it is easily accessible and offers better working conditions for the installation of a large OBS network than other remote ultraslow spreading ridges, for example the SWIR or the Gakkel Ridge.

The Knipovich Ridge is a very oblique (35°–50° between spreading direction and ridge axis trend, Figure 1b) ultraslow spreading ridge with a full spreading rate of 14–17 mm/a (Curewitz et al., 2010; DeMets et al., 2010; Okino et al., 2002). The around 500 km long transform free ridge is bound to the north by the Molloy transform fault. To the south, the ridge axis bends into the Mohns Ridge. The Knipovich Ridge is a very young divergent plate boundary, built within the framework of the opening of the North Atlantic (Kokhan et al., 2012; Okino et al., 2002). Due to the proximity to the continental shelf, the ridge axis and especially magmatically less active sections are covered by up to 950 m thick sediments (Amundsen et al., 2011; Curewitz et al., 2010; Kvarven et al., 2014). Along the Knipovich Ridge only few dredge samples give information on the seafloor petrology. All samples originate from inferred volcanic regions and show basalts (Elkins et al., 2014; Lehnert et al., 2000). The segmentation of the ridge based on morphology, magnetic or gravity data (Curewitz et al., 2010; Okino et al., 2002) reveals major volcanic segments spaced by about 60–110 km that are inferred to be stable for the last 7–8 Ma (Hellevang & Pedersen, 2005). The major volcanic center of the studied ridge section is the Logachev volcanic center (Figure 1b). In a short

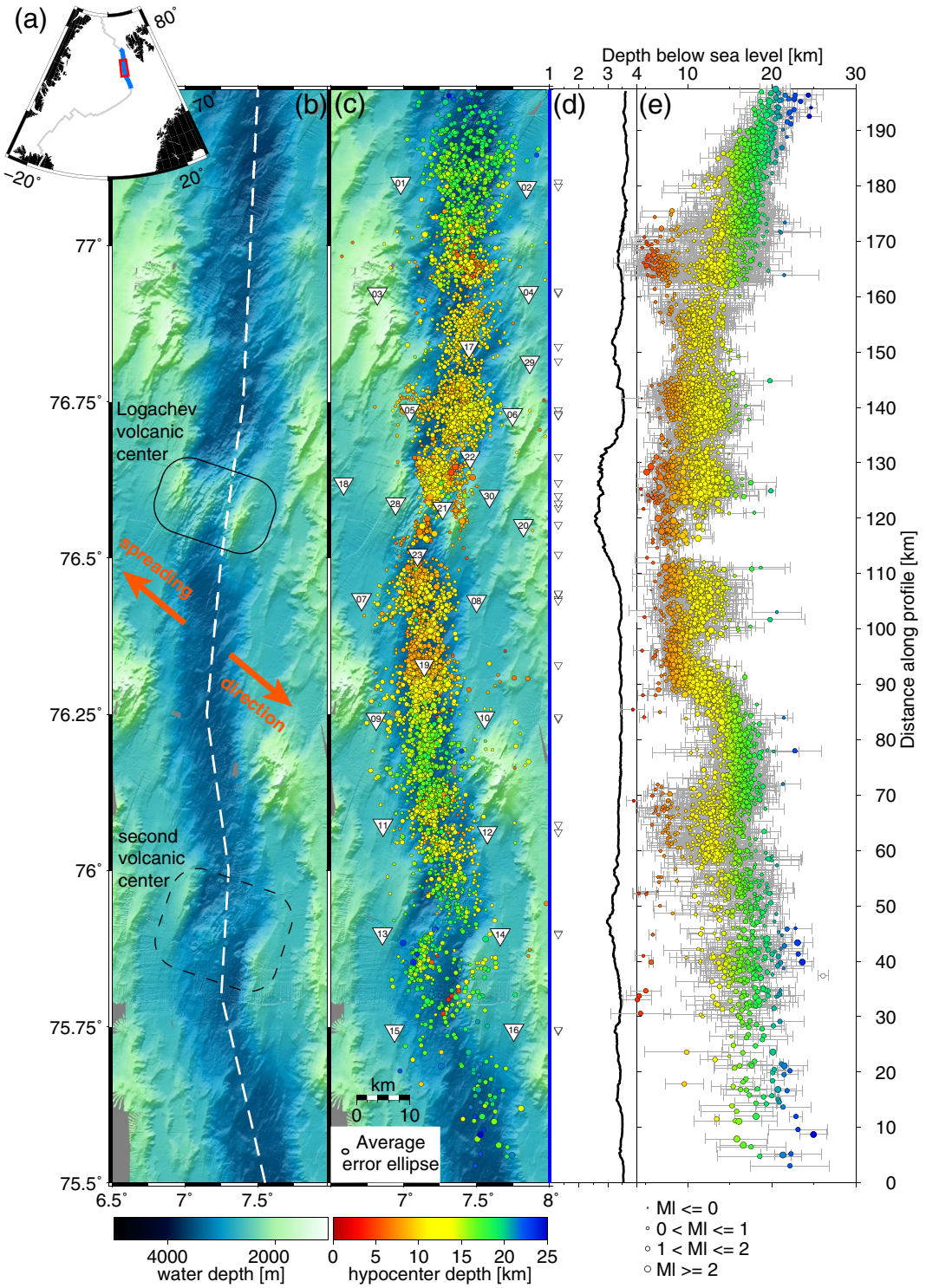

Figure 1. (a) Overview of the Knipovich Ridge (blue) and the study area (red square). (b) Bathymetry of the study area (50 m grid cell size). White dashed line marks profile line of (d and e), orange arrows indicate spreading direction. (c) Earthquake locations (circles) of 8,435 reliable events, color coded according to hypocenter depth and circle size varying with magnitude (Ml), average error ellipse for all events in the lower left corner. OBS stations (white triangles) are labeled with their station number. (d) Superelevated bathymetry along profile with projected stations (triangles). (e) Cross-section along profile with projected earthquake positions limited to events within 6.75°E and 7.75°E. Gray bars indicate depth errors.

term OBS deployment Schlindwein et al. (2013) found shallow hypocenters close by and an aseismic region underneath the Logachev volcanic center. With our new data set of 11 months segment-scale seismicity, we investigate here how melts supply the Logachev volcanic center, how the ridge is divided in sections and how these differ in their deformation modes to contribute to a better understanding of ultraslow-spreading processes at segment scale.

2. Materials and Methods

2.1. Data Sets

2.1.1. Bathymetry Data

We compiled high-resolution multibeam bathymetry data of the study area from several cruises of RV Maria S. Merian, mainly MSM57 (Bohrmann et al., 2017), MSM67 (Damm et al., 2017) and MSM68 (Schlindwein et al., 2017) supplemented by data sets from RV Polarstern cruises, i.a. PS100 (Kanzow, 2017). The new bathymetric compilation covers the ridge axis and about 40 km to both sides of the valley with a resolution of up to 50 m between the Molloy Transform Fault in the north (about 78.5°N) and just south of 75°N (Figure 1b).

2.1.2. Seismological Data

The KNIPAS seismological network consists of 26 OBS that recorded seismicity for about one year along 160 km of the Knipovich Ridge (Table S1, Figure 1c). The OBS were deployed during RV Polarstern cruise PS100 (Kanzow, 2017) in August/September 2016 and recovered during RV Maria S. Merian cruise MSM68 (Schlindwein et al., 2017) in October 2017. All OBS were equipped with HighTech Inc hydrophones (8 kHz–100 s) and, except station KNR21, with Güralp CMG-40T broadband seismometers (50 Hz–60 s). Station KNR21 had a Trillium Compact broadband seismometer (50 Hz–120 s). The sampling rate was either 50 or 100 Hz (Table S1). 23 OBS came from the German DEPAS Pool (Schmidt-Aursch & Haberland, 2017), three OBS were supplied by the Polish Academy of Sciences. The Polish OBS were deployed and recovered by, respectively, RV Horyzont II and RV Oceania. The internal clocks were synchronized before deployment and after recovery. Most of the OBS measured their clock drift rate, for eight stations (Table S1) the clock drift was determined using noise cross-correlation with the procedure described by Hannemann et al. (2014). During the noise cross-correlation a linear clock drift could be verified and was then assumed for all stations, except KNR21 because of different instrumentation. The OBS were deployed in free-fall mode. The position on the seafloor was determined from seismic profiles, where available, and at two-thirds between the deployment and recovery position for the remaining OBS (Schlindwein et al., 2017).

2.2. Earthquake Detection and Picking

We used the Lassie earthquake detector by Heimann et al. (2017). Lassie searches all possible source locations in the survey volume and defines an event if a specified threshold of a characteristic function is reached. We created a reference data set of manually identified earthquakes in 21 days of record distributed over all seasons and adapted the Lassie parameter set such that as many earthquakes as possible were detected while avoiding excessive amounts of false triggers. We used higher weights for the P phases and a detector threshold of 170. The automatic detector achieved a detection of nearly 100% of the manually detected events. The performance was good as long as the network was more or less complete (Table S1). We therefore limited earthquake analysis to end of July 2017, which makes 11 months of data. In total, Lassie detected 18,451 events.

We automatically picked P and S phases using the kurtosis-based PSPicker by Baillard et al. (2014), but the picking results were not satisfactory and needed refinement by manual picking in SEISAN (Havskov & Ottemöller, 1999; Ottemöller et al., 2017). The main reason for the poor performance of the automatic picker are ocean bottom currents that acted on the OBS and produced harmonic tremor signals in the frequency range between 1 and about 10 Hz (Stähler et al., 2018). Filtering records between 7 and 17 Hz achieved the best results. We skipped 265 events without any PSPicker picks to further suppress false detections. The picks of the remaining 18,186 events were refined manually. For picking we assumed pick uncertainties of 0.02 s and 0.1 s for clear and 0.05 s and 0.2 s for emergent P and S picks.

2.3. Velocity Model and Earthquake Location

The 1D velocity model used for location was determined by PyVelest (Kissling, 1995; https://github.com/saeedsltm/PyVelest) in combination with the location algorithm HYPOSAT (Schweitzer, 2001, 2018). We used >1,000 randomly created velocity models (Figure S1) based on start models by Schlindwein and Schmid (2016) and Jokat et al. (2012). With those models we located a subset of 873 earthquakes with at least 20 phase picks. Layer velocities and depths were iteratively adjusted and the algorithm found the best models based on the lowest RMS after three iterations. We selected the 25 best fitting models of the Velest runs for further testing with HYPOSAT. We performed an iterative location procedure with HYPOSAT using the mean stations residuals of each run as pre-set station correction terms for the subsequent run. To calculate the station correction terms, we included only phase readings from earthquakes to a maximum distance of 80 km (half network length) and excluded phases with residuals larger than 1.5 s as incorrect picks. The station correction terms (Table S1) were iterated five times, afterward no enhancement was achieved. The final 1-D velocity model was then selected not only by RMS, but we chose the model that achieved a high number of located events with a depth solution, a low mean RMS, a low mean length of the major axis of the 95% error ellipse (Smaj) and low mean depth error. We tested different Vp/Vs ratios between 1.7 and 1.8 and found that higher ratios result in slightly smaller RMS values, but higher station correction terms, for lower ratios vice versa. As a compromise, we chose a ratio of 1.75. The final model has a velocity of 3.5 km/s at the seafloor at a reference depth of 3,389 m (Figure S1). If not stated otherwise, depths are given below sea-level. Velocities quickly increase with depth reaching 6 km/s at about 4.5 km in agreement with the crustal thickness (Jokat et al., 2012) and the preliminary results of the refraction seismic study. A velocity of 8.08 km/s is reached at 25 km depth. In general, the different velocity models tested with HYPOSAT gave similar earthquake patterns.

Inspection of phase residuals per station over time showed systematic trends for station KNR21, caused by a nonlinear drift of the OBS clock. Therefore, we split the station correction terms for this station into three periods and applied different values (Table S1).

For verification of the HYPOSAT locations, we performed location runs using NonLinLoc (Lomax et al., 2000), which uses a probabilistic location approach. We used two different misfit functions and the fixed station corrections determined for HYPOSAT with the iterative procedure described above. The hypocenter patterns are very similar (Figure S2), except at the margins of the network, where station cover decreases. Here, NonLinLoc solutions produce larger hypocenter depths than HYPOSAT, a larger scatter in hypocenter depths and diverging results between the two misfit functions. Therefore, we decided to use HYPOSAT solutions for further analysis.

All 14,938 earthquakes with at least four picks were then located. We received 14,915 located events, of which 14,401 events are within the study area (Figure S3). We consider 8,435 events with an epicentral location error (Smaj) and a depth error of less than 5 km and a maximum RMS of 0.4 s as reliably located. The subset of well-located events achieved a mean RMS of 0.22 s and a mean horizontal and vertical location error of 1.3 and 1.5 km, respectively (Table S2).

2.4. Magnitudes and *B*-Values

Amplitudes were picked automatically on vertical component seismograms where available (Table S1). Stations with large scatter in amplitude readings were discarded. Local magnitudes were calculated subsequently using the formula by Bullen and Bolt (1985) with hypocentral distance instead of epicentral distance. In our data set the epicentral distance is often significantly smaller than the hypocentral depth and might therefore underestimate attenuation effects.

Calculation of the *b*-values is based on the Gutenberg-Richter relation (Gutenberg & Richter, 1944). To receive more robust results, we calculated the magnitude statistics on a larger subset of 12,852 earthquakes with inverted depths, a maximum depth error of 5 km and a Smaj of maximum 10 km. For the determination of the completeness magnitude Mc we used the maximum curvature approach (Wiemer & Wyss, 2000; Wyss et al., 1999) resulting in Mc 0.7. Since this approach tends to underestimate the completeness magnitude, we also used the *b*-value stability approach (Cao & Gao, 2002; Woessner & Wiemer, 2005), which tends to overestimate the completeness magnitude, resulting in Mc 1.0. We used the higher completeness

magnitude 1.0 to ensure a complete catalog. We calculated the *b*-value for three sections of the study area to reveal seismicity differences (Figure S4).

2.5. Fault Plane Solutions

For the determination of fault plane solutions, we selected a subset of earthquakes with M > 2, a maximum azimuthal gap between recording stations of 180° and at least 10 P phase picks. For two regions of particular interest (between stations KNR01-KNR02-KNR06-KNR05 and KNR19-KNR09-KNR13-KNR14-KNR10) we also examined earthquakes with M > 1.5 and 6 or more P phase polarities resulting in 190 events altogether. After manual first motion picking we used FOCMEC (Ottemöller et al., 2017; Snoke et al., 1984) for the calculation. We prohibited polarity errors and identified well-defined, stable solutions by testing different search parameters. Only solutions without significantly different focal mechanisms were used for interpretation. Altogether we obtained 44 well-determined fault plane solutions, which we divided into five groups according to their type of mechanism and strike direction (Chapter 3.7). Velocity model and location errors influence the solution. Therefore, we do not use single fault plane solutions or strike and dip values for interpretation, but only the entirety of fault plane solutions.

3. Seismicity Patterns in Space and Time

Our data set gives for the first time an impression of the microseismicity along an extended section of a mid-ocean ridge covering almost 200 km of ridge axis and entire spreading segments (Figure 1). We describe and analyze the seismicity and related spreading behavior on segment-scale. Most of the seismicity occurs within the rift valley, while the maximum hypocentral depths vary significantly along axis. The seismicity is also not distributed equally along the axis, but exhibits more and less active ridge portions.

3.1. Maximum Depth of Faulting

A very obvious and variable feature of seismicity is the sharply defined lower boundary, which delineates the maximum depth of faulting (Figure 1e), independently of the type of faulting. This boundary is shallowest at the Logachev volcanic center and the surrounding areas from profile km 95–160, where earthquakes occur only down to 15 km (Figure 2). North of km 160 the maximum hypocenter depths increase constantly to about 25 km depth at the end of the cross-section (Figures 1e and 2). South of km 95 maximum depths are typically around 20 km with slightly deeper events south of km 50. While the lower limit of seismicity increases more or less continuously north of km 160, local undulations with shallowing seismicity (e.g., km 65, 95, or 135) disrupt the large-scale pattern of maximum depth of faulting south of km 160.

3.2. Shallow Seismicity

Our network design with a station spacing of about 20 km along the ridge and additional stations around the central volcanic edifices was not optimized for shallow seismicity. However, we register shallow seismicity not only in regions with higher station density, but also in the south between km 55 and 70 along the profile and in the north between km 160 and 175, where station spacing is large. In addition, we also observe regions without shallow seismicity despite a denser station cover, for example around km 150 along the profile. Therefore, the distribution of shallow seismicity as described in the following is not severely influenced by the station geometry.

The upper boundary of seismicity is very variable along the rift axis. The seismicity mostly sets in at depths of 7–8 km (Figure 2), ~4 km below the sea floor and is present in almost the entire survey area at a depth level of 10–15 km. In contrast, shallow seismicity in the upper 4 km of the lithosphere is less continuous and confined to specific areas. Around km 165 along the profile, a well-defined cluster of shallow earthquakes occurs at a depth of around 5–8 km. This cluster is clearly detached from the continuous seismicity band below at depths between 10 and 17 km (Figure 1e). Southward shallow earthquakes are absent for about 20 km along the profile (km 145–165). In the central study area between km 90 and 145 along the profile, diffuse shallow seismicity is present. Seismicity is clustered around the volcanic center, in the surrounding areas the pattern is more diffuse. South of km 85 along the profile shallow seismicity stops and picks up at

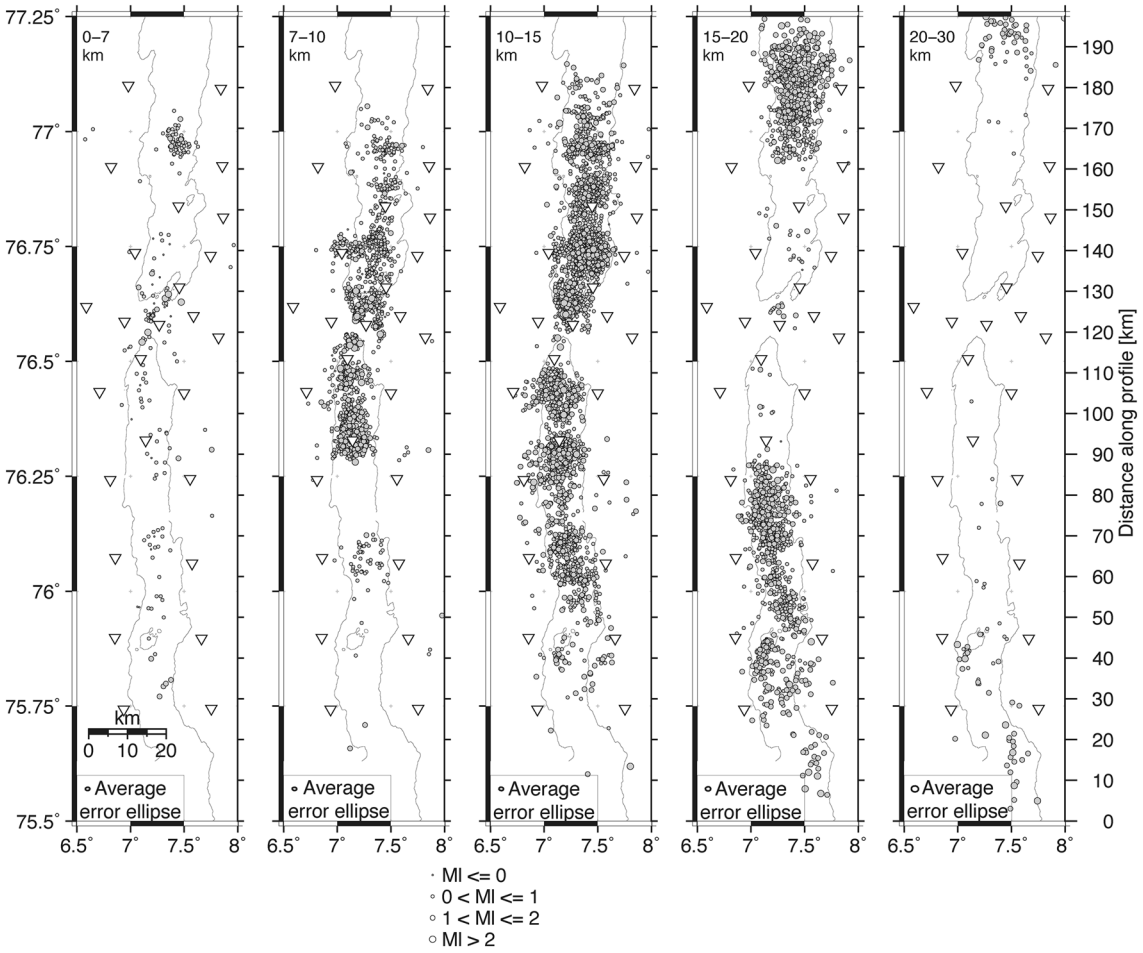

Figure 2. Map view of earthquake activity in different depth levels. The rift valley is marked by the 3,000 m water depth contour. Labels and symbols as in Figure 1.

km 70 with a broad and diffuse scatter around 7 km depth (Figure 1d). This pattern can possibly resemble a detached shallow earthquake cluster similar to km 165 along the profile. Further south few shallow earthquakes are spread at depths lower than 5 km.

3.3. Aseismic Regions

A prominent feature of the seismicity distribution are distinct areas lacking earthquake activity. These aseismic areas are not a function of earthquake selection, but also show up as aseismic without selection based on location quality (Figure S3). We further argue that lateral variations in seismicity and the occurrence of aseismic areas is not a function of network geometry, since the backbone of the network consists of station pairs at both sides of the rift valley regularly spaced by about 20 km.

3.3.1. Logachev Aseismic Region

One very obvious aseismic region is located beneath the Logachev volcanic center stretching ~10 km along axis between km 110 and 120 along the profile (Figures 1b and 1c). This aseismic region has tentatively circular shape with relatively clearly defined edges across the entire depth scale. An exception is the seismic activity directly in the center of the gap at depths between 7 and 10 km. This seismicity occurs mostly in short time periods as swarms (Chapter 3.6).

3.3.2. Aseismic Regions in the Upper Lithosphere

A very distinct aseismic region is located between km 70 and 90 along the profile, Figures 1e and 2). It is ~20 km long and the seismicity band sets in at depths up to 15 km. The underlying seismicity band has a relatively constant vertical extension of about 5 km, with subparallel upper and lower limits. The edges of the aseismic region toward the north and south differ in their steepness (Chapter 3.3.3) and shallow earthquake activity (Chapter 3.2).

At the northern edge of our survey area, we observe a similar aseismic zone in the upper lithosphere with a continuous band of deepening seismicity below. Stations KNR01 and KNR02 (km 180 along the profile) are situated near the southern limit of this zone but would have detected any shallow seismicity at least as far north as km 185. Hence, we suggest that an even more pronounced aseismic area may extend beyond the northern limit of our network.

3.3.3. Lateral Seismicity Disruptions

We identified regions with lateral seismicity disruptions, where seismicity becomes less dense and its depth spread decreases (Figure 1e). Here, earthquakes mainly occur at depths around 10 km, while seismicity instantly ceases toward shallower and higher depths and thereby narrowing the seismicity band. One such lateral seismic disruption is found at km 150 along the profile. Shallow seismicity is absent in this area and seismicity begins at depths of 9 km, whereas shallower seismicity is present north- and southwards. Similarly, a lateral seismicity disruption is found at km 160. The lateral seismicity disruptions show a SW-NE trend in the map (Figure 1c). A similar but less prominent lateral seismicity disruption is found at km 130 along the profile. It is masked by several shallower events, especially toward the Logachev volcanic center, and does not show a clear directional trend in the map.

Another form of lateral seismicity disruption is seen in the map (Figure 1c) as an area with little seismic activity at km 45 along the profile extending northwest-southeast. This disruption shows nearly no seismic activity over the entire depth section and might therefore be similar to the aseismic region underneath the Logachev volcanic center.

In the cross-section a unique form of seismicity disruption is found at the southern end of the long aseismic region at kilometers 70 to 90 along the profile (Figure 1e). Here, the band of deep seismicity is almost cut off and replaced toward the south with a different depth distribution of earthquakes whereas northward, the seismicity band shoals more gradually.

3.4. Earthquake Swarms

Several earthquake swarms were observed around the Logachev volcanic center (Figure 3). We defined earthquake swarms visually by an abrupt steepening in the cumulative event curve (Figure S5) coinciding with an event cluster in time and space of at least 10 events in total.

Only two swarms were observed outside the Logachev area: around km 95 and km 180 along the profile (Figure 1). Enhanced seismicity occurs at km 95 at the end of February 2017 for three days consisting of 40 events with magnitudes between −0.1 and 1.1. The area of activity is large compared to the swarm activity in all other locations with depths of around 4–8 km. At km 180, swarm activity occurred from October 6 to 9, 2016 with 20 events of magnitudes −0.9 to 2.4. The swarm occurred at about 20 km depth close by the eastern rift flank on a ridge crest oriented perpendicular to the spreading direction.

All other earthquake swarms were detected in the Logachev area (Figure 3). The region with the highest swarm activity is the northern side of the Logachev volcanic center, directly at the northern edge of the aseismic region (Chapter 3.3). Here, swarms occur in September, October and November 2016 and in January, March and May 2017. Each swarm lasts for 1–7 days, mostly 3 days, and magnitudes vary between −0.9 and 2.1. The mean number of events per swarm is 32. The highest magnitudes per swarm do not occur at the start of the swarms and second highest magnitudes are only slightly smaller, deviating from mainshock-aftershock activity.

The most prominent earthquake swarm is situated in the aseismic region underneath the Logachev volcanic center. It marks the only significant activity within the aseismic region and is limited to five days in March

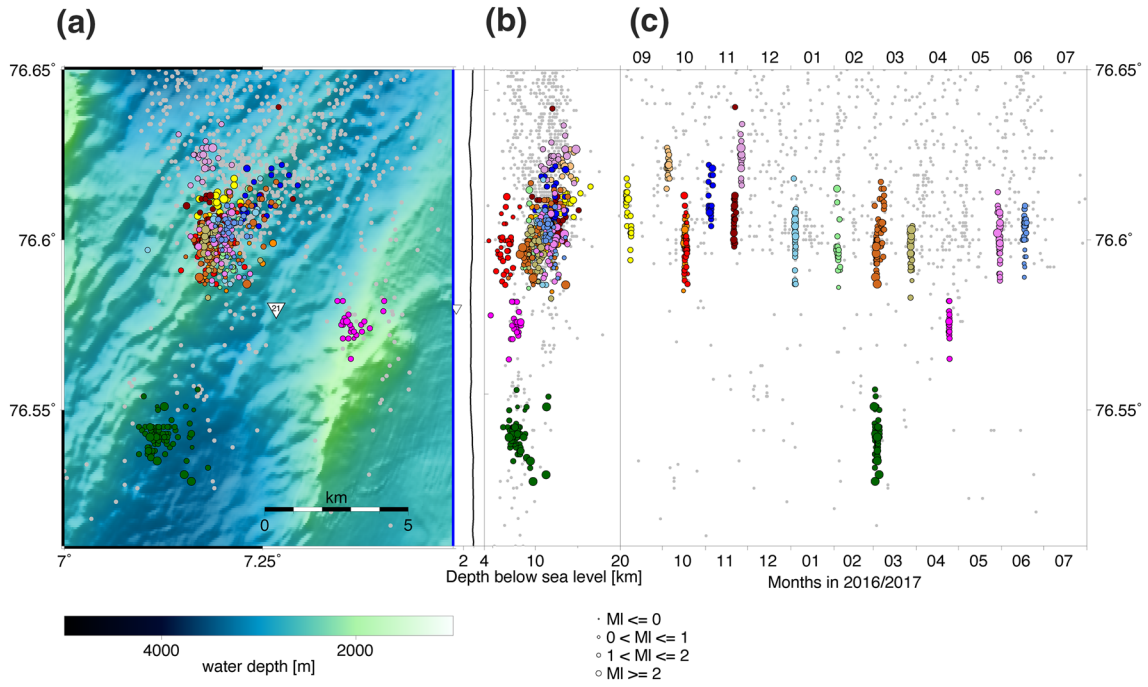

Figure 3. Earthquake swarms in their spatial and temporal occurrence. Labels and symbols as in Figure 2, swarm earthquakes are colored according to swarm. (a) Map, (b) cross-section with bathymetry and (c) latitude over time.

2017. The swarm extends at depths between 6 and 12 km. Magnitudes of the 74 events are between −0.5 and 1.9. One month later, in April 2017, on the neighboring ridge crest another smaller earthquake swarm occurred with 24 events of magnitudes of −0.1–1.16 during one day.

3.5. Faulting Mechanisms

We describe the focal mechanisms in five summarizing groups (Figure 4). We only obtained fault plane solutions for earthquakes at depths between 11 and 21 km, since these events produced clear phase arrivals at sufficiently many stations.

Surprisingly, the largest number of fault plane solutions shows reverse mechanisms despite the general diverging nature of the plate boundary. The strike of the fault plane solutions varies between NNW-SSE and NNE-SSW. The mean dip of the faults is 45° and most of the mechanisms do not show any or very small oblique motion. About 80% of the reverse faulting events occur south of the Logachev volcanic center, only three events with reverse mechanisms are found scattered north of it. South of km 85 along the profile reverse faulting is the predominant type with many similar and consistent mechanisms. All reverse faulting mechanisms tend to occur close to the rift valley flanks.

The second largest group of focal mechanisms are normal faults with strikes approximately SW-NE, while for most the strike is SSW-NNE, perpendicular to the spreading direction. The mean dip is 45.5°. While this focal mechanism agrees best with the large-scale tensile stress regime of the ridge, only about a third of our focal mechanisms belong to this group. The events mostly occur north of km 145 along the profile and some are scattered along the ridge section. Representatives of this group mainly occur within the rift valley, but are also found at the rift axis flanks.

In the second group of normal faulting mechanisms, the strike is NW-SE, about perpendicular to the other group of normal faulting mechanisms. Three of the four representatives occur very close to each other around km 140 along the profile. The last event is located south of the Logachev volcanic center in the rift valley.

A strike-slip faulting mechanism is found only once in our data set, but faulting mechanisms with significant oblique motion have been grouped as strike-slip mechanisms as well. The strike-slip mechanisms

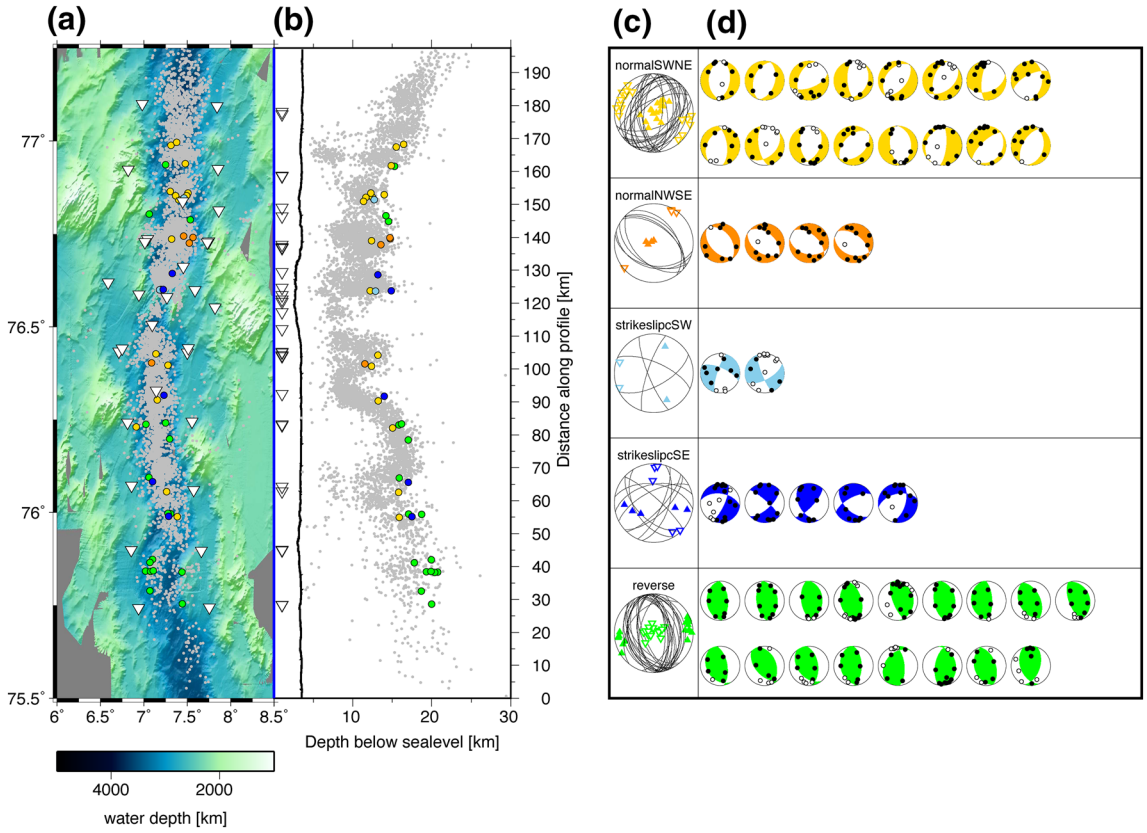

Figure 4. Fault plane solution groups and their location. (a) Map and (b) cross-section with earthquakes (gray circles) and fault plane solutions in colors according to mechanism group. (c) Combined fault plane solutions with group names, P-axes (filled triangles) and T-axes (unfilled inverted triangles). (d) Single fault plane solutions (colored quadrants are compressional) with compressional (black dots) and dilatational first motion picks (white dots).

are split into two groups indicating the compressional quadrant in the SW or SE. The classic strike-slip mechanism with compression in the SW is located at the Logachev volcanic center, surrounding are representatives of other groups, that is two strike-slip mechanisms with compression in the SE and one normal faulting mechanism, which is similar to the two strike-slip ones, but with less oblique motion. Other strike-slip mechanisms occur along the entire rift axis and often close to other mechanisms. Fault plane solutions for swarm earthquakes do not exists, because these events did not fit our selection criteria.

4. Discussion and Interpretation

Seismicity patterns are highly variable along the nearly 200 km long studied ridge section suggesting a variety of processes and high complexity in the area.

4.1. Off-Axis Seismicity

Teleseismic earthquake catalogs for the Knipovich Ridge show a considerable amount of off-axis seismicity to both sides of the rift valley with a majority of events to the east in the direction of Svalbard (Schlindwein et al., 2015; Zarayskaya, 2017). In our data set only few earthquakes are recorded off-axis. The differences in these data sets could be explained by the poor station distribution of the permanent land stations, that is in Svalbard and Greenland. Gibbons et al. (2017) showed that with improved location algorithms and velocity models many events get located along the spreading ridge. Nevertheless, a small number of events is still located mainly eastward of the rift valley. In our local data set, we located few off-axis events, also mainly to the east of the rift valley. Those events are not distributed equally, but occur north of the Logachev volcanic center mainly on the eastern side, then swap over to the western side and back to the eastern side at the end

of the Logachev section. The off-axis seismicity does not seem to be directly affected by the activity along the ridge, but might be an effect of the sediment loading (Libak et al., 2012).

4.2. Large Scale Melt Focusing

The study of seismicity along the Knipovich Ridge opens up new perspectives on the segmentation of this ridge (Figure 5). Up to date, segmentation of the Knipovich Ridge is mainly based on morphology, magnetic or gravity data with volcanic centers spaced by about 20–40 km including major and subordinate volcanic centers (Curewitz et al., 2010; Okino et al., 2002), with Logachev volcano as major volcanic center. The seismic network covered several such volcanic centers to study segment-scale processes, and reveals a refined seismological segmentation pattern with larger segments divided into sections that further show smaller subsegments.

The variability in the maximum hypocenter depths defines one ~70 km long section (km 90–160, Figure 5) with maximum hypocenter depths up to 15 km around the Logachev volcanic center, which we consider to be currently magmatically active. From this central magmatic section, hypocenters deepen by more than 10–25 km depth at distances of about 70 km to either side defining one large segment of about 140 km extent. The lower boundary of the seismicity band defines the transition from brittle to ductile deformation at an isotherm with temperatures thought to be in the range of 600–650°±100° (Anderson, 1995; McKenzie et al., 2005). Assuming no heat production within the oceanic lithosphere, the isotherm marking the LAB can be assumed to display similar topography.

Sauter and Cannat (2010) argue that volcanic centers at ultraslow spreading ridges receive more melt than the regional average and a melt focusing mechanism must be in place to distribute melt along the axis. It has been suggested that melt may travel along a permeability boundary near the LAB upwards toward volcanic centers (Cannat et al., 2003; Montési et al., 2011; Standish et al., 2008), but it is unclear over which distances this is possible. Marked feature of ultraslow spreading ridges are major volcanic centers spaced at about 100 km distance and subordinate centers in between. At the SWIR Standish et al. (2008) found distances of up to hundreds of kilometers between two major volcanic centers and postulate melt focusing over such distances. Cannat et al. (2003) termed segments #8 and #11 major volcanic centers with a distance of 70 km between the segment centers. Along the Gakkel Ridge distances between large volcanic centers are 50–160 km (Michael et al., 2003). The Knipovich Ridge exhibits larger volcanic centers spaced at 60–110 km (Hellevang & Pedersen, 2005; Okino et al., 2002). Hellevang and Pedersen (2005) suggest that this large-scale segmentation is stable over at least the last 7–8 Ma. From our segment-scale seismicity survey we present evidence for a seismicity band that shows a continuous trend of shallowing hypocenters toward a major volcanic center. The long wavelength undulation of the LAB suggests that melt could travel as far as 70 km along axis within one segment toward its volcanic center, where the asthenosphere shallows and melts can ascent to the surface.

Similar to our observed aseismic region underneath the Logachev volcanic center, Schmid et al. (2017) found a temperature controlled aseismic region hosting a melt reservoir underneath the Segment 8 volcano at the SWIR. Swarm activity observed at the Segment 8 suggests ongoing magmatism (Meier & Schlindwein, 2018; Schmid et al., 2017). In analogy, swarm activity at the northern flank of the Logachev volcanic center is probably also related to ongoing magmatic activity during the entire duration of observation. Moreover, at the northern flank of the Logachev volcanic center fresh basalts were found (Elkins et al., 2014; Lehnert et al., 2000). We therefore speculate that the Logachev volcanic center is currently active.

Sauter et al. (2001) suggest melt feeding into subordinate volcanic centers occurs from a central volcano. Schmid et al. (2017) found evidence for intrusion activity 60 km away from the Segment 8 volcano into the neighboring segment. Swarms in our study area are only seen in the vicinity of the volcanic center and within the surrounding 10 km. Therefore, we do not see obvious feeding processes at present time and we cannot assure if the subordinate volcanic centers are fed from the central volcano. Along the Knipovich Ridge the high ridge obliquity might serve as a barrier for melt feeding processes along the spreading axis. Indication for a sub-segmentation hindering further feeding are the pronounced along axis variation of hypocenter depths of up to 5 km within the central magmatic section.

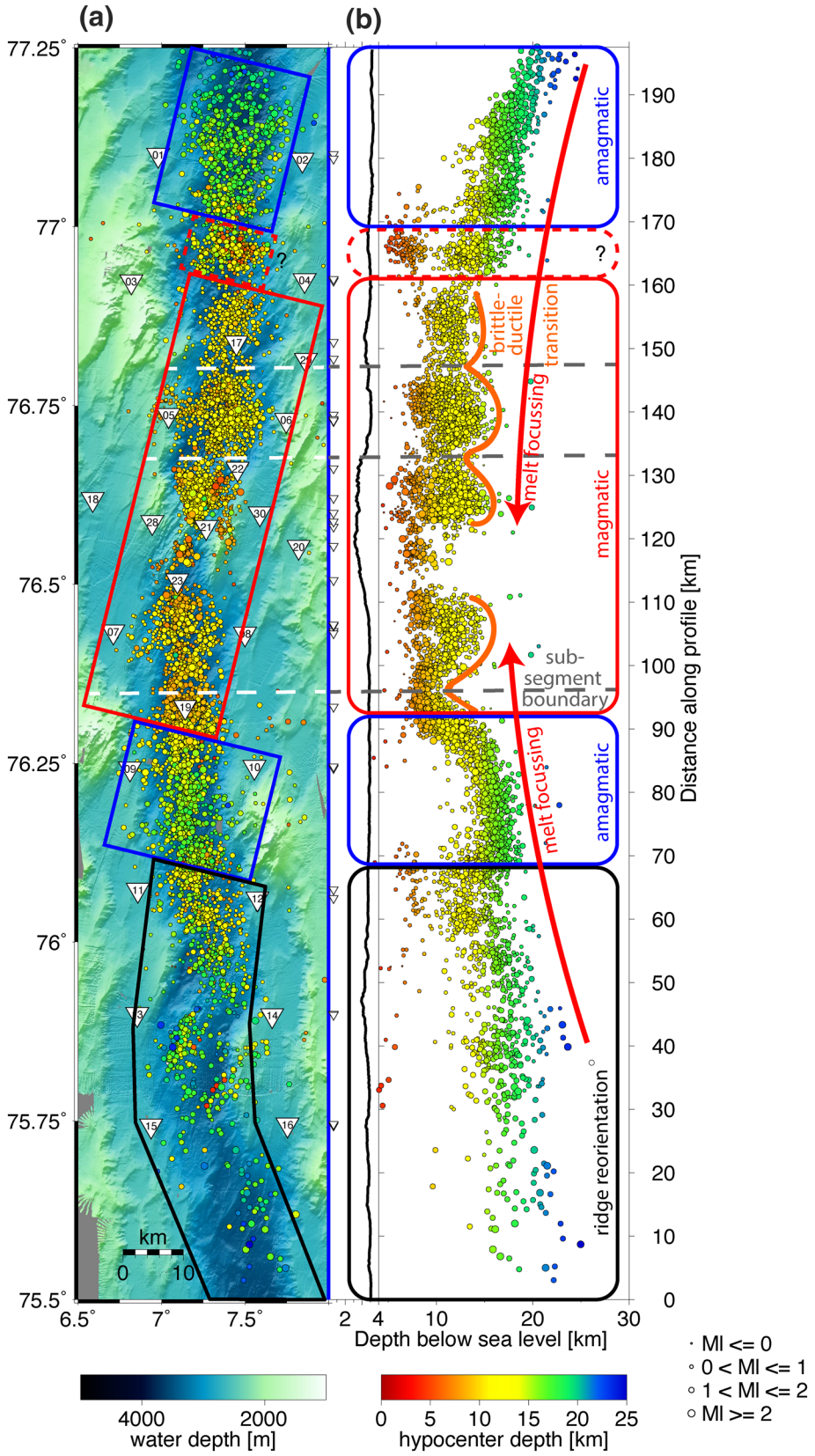

Figure 5. Sketch of interpreted characteristics and processes in (a) map view and (b) cross-section. Labels and symbols as in Figure 1.

4.3. Magmatic and Amagmatic Spreading Styles

From the seismicity styles we distinguish magmatic sections and areas with reduced magmatism (Figure 5), which we term here amagmatic, although the few dredge samples obtained along the mostly sediment covered Knipovich Ridge exclusively recovered basalts. Hence, there is no evidence for exposure of mantle rocks, but sampling did not cover amagmatic areas. A comparison of the characteristics of the central magmatic and the amagmatic sections is shown in Figure 6.

4.3.1. Magmatic Section

The central magmatic section is characterized by relatively shallow maximum hypocenter depths and seismicity occurring throughout the entire depth interval, including earthquakes in the crust, which is 5.7 km thick at the Logachev volcanic center (Jokat et al., 2012). Seismicity seems to be stable in time, since similar seismicity throughout the depth range was observed in a 10-days OBS study in 2009, although the location accuracy is less and the magnitudes are larger than in the present study (Schlindwein et al., 2013). High *b*-value with a high portion of small earthquakes (Figure S4) is typical for seismicity driven by magmatic processes (Bohnenstiehl et al., 2008; Tolstoy et al., 2001). The direction of the least compressive stress is also reflected in the normal faults striking (sub-) perpendicular to the spreading direction. Other observed faulting mechanisms or directions map the higher tectonic complexity compared to the global CMT catalog (Ekström et al., 2012), which nearly exclusively shows the large-scale divergent motion on larger fault planes. Depth distributions of earthquakes, which peak around 8 km depth below seafloor (bsf, below reference depth of 3,389 m) indicate a strong lithosphere at magmatic sections in agreement with the conceptual strength profiles suggested by Cannat et al. (2019) for volcanic seafloor at the SWIR (Figure 6d and Chapter 4.3.2). The transitions from the central magmatic section to the amagmatic sections occur on short distances of about 10 km. Similar juxtaposing of magmatic and amagmatic spreading has been observed by Cannat et al. (2019) at the SWIR. The abrupt change of characteristics might be a result of a change in composition. At the northern magmatic-amagmatic transition, shallow earthquakes (Figure 5, km 155–170) occur underneath two small volcanic cones within the rift valley, inbetween only few earthquakes occur. This resembles the Logachev volcanic center at smaller scale and might be a recent development of building a new volcanic center, thereby adding complexity to the segmentation pattern. A second possibly magmatic section in the south of our study area (Figure 5, ridge reorientation section) shows a more complex seismicity pattern and will be discussed in Chapter 4.3.3.

4.3.2. Amagmatic Sections

The deeper maximum hypocenter depths and a remarkable lack of shallow seismicity are the main characteristics of the sections that we term amagmatic (Figures 6a and 6c). Schlindwein and Schmid (2016) observed comparable aseismic regions in the upper lithosphere in areas of known mantle rock exposure, although earthquake locations are less well defined than in this study. This suggests that a lack of shallow seismicity may occur at more locations along ultraslow spreading ridges. The boundary marking the onset of faulting at 10–15 km depth runs parallel to the temperature-controlled brittle-ductile boundary, suggesting that it is likewise controlled by temperature. Following Cannat et al. (2019), we constructed conceptual lithospheric strength profiles in comparison to the observed seismicity (Figure 6d). Assuming that the long-term mechanical behavior of the lithosphere is reflected in its short-term deformation (Burov, 2011; Ranalli, 1995; Scholz, 2002), earthquake depth distributions have been used as proxy for the strength of the lithosphere (Albaric et al., 2009; Déverchère et al., 2001). We used the same rheology and rock composition for magmatic and amagmatic sections (Byerlee's law [Byerlee, 1978], Byerlee's law modified for serpentinization [Escartin et al., 1997], and power law creep [Ranalli, 1995]). By varying the temperature gradient and the depth of serpentinization, we could produce lithospheric strength profiles for magmatic and amagmatic sections resembling the earthquake depth distribution. We therefore suggest in agreement with mantle velocities <8 km/s in the velocity model that the lack of shallow seismicity may reflect serpentinization of mantle rocks (Carlson & Miller, 2003). Escartin et al. (2001) suggest that already 10% serpentinite drastically reduce strength such that low-level serpentinization down to 9 km depth could explain the lack of shallow seismicity in amagmatic sections. Cannat et al. (2019) argue that not necessarily serpentinization but also the presence of talc may weaken the lithosphere in amagmatic sections. The depth extent of alteration is a function of temperature and availability of water. Mével (2003) suggested hydration at slow and ultra-slow ridges may occur up to

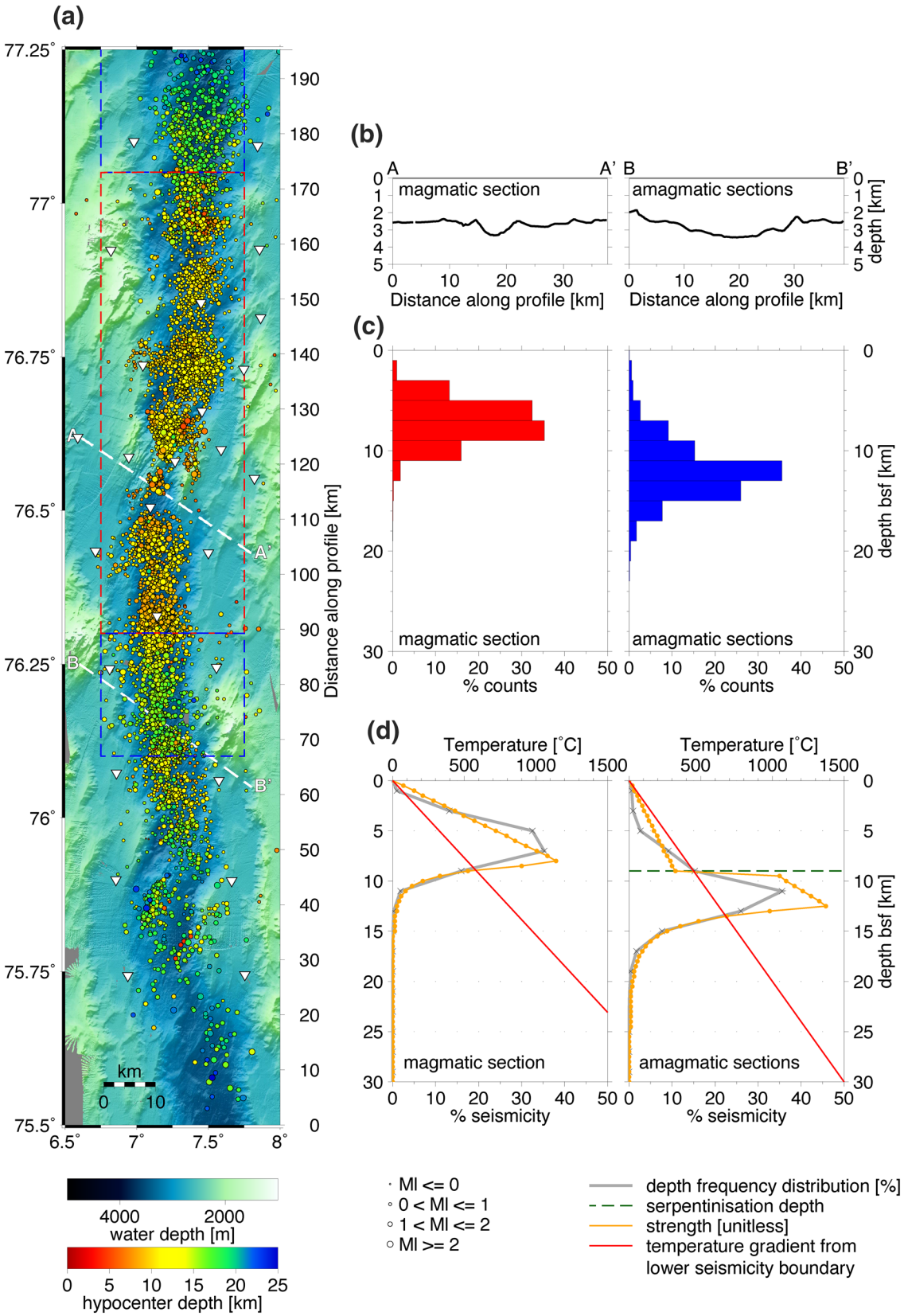
(a)
77.25°
77°
76.75°
76.5°
76.25°
76°
75.75°
75.5°
6.5°
7°
7.5°
8°
A
A'
B
B'
km
0 10
Distance along profile [km]
190
180
170
160
150
140
130
120
110
100
90
80
70
60
50
40
30
20
10
0
4000 2000
water depth [m]
0 5 10 15 20 25
hypocenter depth [km]
(b)
A A' B B'
magmatic section
amagmatic sections
depth [km]
Distance along profile [km]
Distance along profile [km]
(c)
magmatic section
amagmatic sections
% counts
% counts
depth bsf [km]
(d)
Temperature [°C]
Temperature [°C]
magmatic section
amagmatic sections
% seismicity
% seismicity
depth bsf [km]
Ml <= 0
0 < Ml <= 1
1 < Ml <= 2
Ml >= 2
depth frequency distribution [%]
serpentinisation depth
strength [unitless]
temperature gradient from
lower seismicity boundary

the 500°C isotherm, Cannat et al. (2019) in their conceptual sketches use a temperature of 400°C. Assuming a constant temperature gradient and temperatures of 650°C at the brittle-ductile boundary in 13 km depth, temperature at 9 km depth can be estimated to be about 450°C in agreement with the suggested isotherms limiting alteration. If seismicity can be taken as a depth indicator of serpentinization, the deepest parts exhibit deeper reaching alteration than previously observed. Cannat et al. (2010) and Momoh et al. (2017) suggest that serpentinization reaches depths of 4–6 km. Seismicity along potentially serpentinized detachments sets in at 9 km depth (Parnell-Turner et al., 2017), or shallower at 2–5 km (deMartin et al., 2007; Tao et al., 2020).

It may be a function of seismicity survey, whether regions of serpentinization are seen as aseismic. Horning et al. (2018) show serpentinization to result in seismicity around 2–5 km depth, but at magnitudes below the detection threshold of this network. Nonetheless, the suggested *b*-value of 1.7 is comparable to our *b*-value of 1.59±0.07 of both amagmatic sections (Figure S4). Serpentinization related weak seismicity may be present, but not detectable by our network. Grevemeyer et al. (2013) argue that serpentinized faults may be strong; however, at the magnitude level we consider here, no seismicity is seen. Another possibility is that excessive serpentinization is currently not active and we observed a time period of silent deformation in previously serpentinized areas. A lack of shallow earthquakes down to 4–9 km depth is also observed on detachment surfaces (deMartin et al., 2007; Parnell-Turner et al., 2017). Cannat et al. (2019) associate detachment faulting with corrugated seafloor type mode differing from smooth seafloor, for which they expect weaker lithosphere to deeper levels. Although the seafloor is not exposed due to the high sedimentation we assume to encounter here rather latter type with weaker lithosphere (see also Section 4.4).

4.3.3. Ridge Reorientation Section

The southern amagmatic section probably ends around km 60–70 along the profile (Figure 5). The interpretation of the region further south is speculative, as the network suffered from reduced recording times and component failures of the southernmost stations, such that the number of detected earthquakes was smaller. Nevertheless, the seismicity pattern is still distinctive. In the bathymetry, we find rough seafloor and an insinuated volcanic ridge, which is interpreted as a magmatic center by Curewitz et al. (2010) and Okino et al. (2002). Most earthquakes are located underneath the axial high, leading to an asymmetrical distribution of seismicity similar to the Logachev volcanic center. On the other hand, we clearly see deeper hypocenters accompanied by few shallow earthquakes, which is a clear contrast to the seismicity pattern along the central magmatic section. The fault plane solutions show exclusively reverse faulting. Coinciding in this area is the change of the spreading ridge orientation at km 35 along the profile from a strike of 000–007° in the north, while south it is 343–350° (Curewitz et al., 2010). In this complex setting, a higher supply of magma would support the reorientation of the axis toward a perpendicular orientation relative to the spreading direction (Cannat et al., 2008). However, higher magma supply should result in shallower earthquake hypocenters in contrast to our observations. The change of the ridge axis orientation can lead to a very complex, compressive tectonic regime, where reverse faults build the main stress release mechanism. The lower *b*-value of 1.36±0.08 suggests a higher amount of high-magnitude events and thus a more tectonic character. The reorientation process would need a deeper driving mechanism for the rift axis reorientation. Since the Knipovich Ridge is seen as a young and currently still forming plate boundary with a complex and not completely understood evolution history (Kokhan et al., 2012; Okino et al., 2002), the source for a deeper driving mechanism might lay in the ridge's evolution as part of the opening in the North Atlantic. From our observations we cannot distinguish, if this section belongs to the magmatic or amagmatic type, but we suggest that the reorientation of the ridge axis overprints the typical characteristics and therefore has to be treated separately.

4.4. Detachment Faults

Detachment faults accommodate spreading in melt-poor ridge sections along ultraslow spreading ridges (Cannat et al., 2019; Reston & McDermott, 2011). According to Cannat et al. (2019) those steepening

Figure 6. Comparison of characteristics of magmatic (red) and amagmatic (blue) sections. Labels and symbols of the map (a) as in Figure 1. White dashed lines show positions of bathymetric profiles for (b). (b) Bathymetric cross-sections of the rift valley for magmatic (left) and amagmatic (right) sections. (c) Depth frequency distribution of earthquakes for magmatic (left, red) and amagmatic (right, blue). (d) Conceptual lithospheric strength profile (orange) in comparison to the depth frequency distribution of earthquakes (gray) with serpentinization depth (green dashed line) and temperature gradient (red, inferred from the lower boundary of seismicity at 650°C).

downwards normal faults play an important role along the melt-poor or melt-free segments of the SWIR by accommodating almost the entire plate divergence (Sauter et al., 2013). Detachment faults have been observed in seismicity patterns along the SWIR by Yu et al. (2018) and Tao et al. (2020) as dipping plane of hypocenters underneath the rift valley or in similar pattern along the Mid-Atlantic Ridge (MAR; deMartin et al., 2007; Parnell-Turner et al., 2017). Along the MAR Parnell-Turner et al. (2017) analyzed the stress regime of a detachment fault using microseismicity. The dip from fault plane solutions between 50 and 70° is high, Cannat et al. (2019) found fault plane dips of 50° in initial state and reducing to 25° during ridge evolution. Along the Knipovich Ridge, we could not identify regions of enhanced seismicity, where hypocenters concentrate along dipping structures. The mean dip of our normal faults striking NNE-SSW is 45° varying between 20 and 70°. Since this includes fault plane solutions of the entire study area and normal faulting often occurs close to other faulting mechanisms, we cannot define a position of a detachment. Only north of km 140 along the profile normal faults striking NNE-SSW are dominant.

A further characteristic of detachment produced seismicity in teleseismic and hydroacoustic records are enhanced seismicity levels and asymmetric distribution of seismicity (Escartin et al., 2008; Simão et al., 2010). Simão et al. (2010) find symmetric distribution along magmatic segments, while amagmatic segments typically show asymmetric distribution of seismicity attributed to detachment faulting. We observe such asymmetric distribution within the active central magmatic section. The volcanic ridges of the Logachev volcanic center stretch suborthogonally to the spreading direction toward both rift valley boundaries. At the northern flank of the volcanic center seismicity occurs west of the ridge, while in the south seismicity jumps to the eastern side of the ridge. Swarm activity occurs mainly underneath the axial volcanic ridges. Similar seismicity jumps also occur at the smaller ridge extending between stations KNR05-KNR17-KNR04 coinciding with a seismically less active area. Along the other sections we find clear asymmetry between stations KNR13-KNR16, but the fault plane solutions show exclusively reverse faulting, indicating the opposite movement than expected for detachments. None of these asymmetric areas revealed seismicity concentrated on dipping planes that would yield direct evidence for detachment faulting. Hence, from our seismicity data, we cannot identify detachment faults along the studied ridge section. Further seismicity studies with dense networks are needed to characterize the earthquake activity of detachments of various sizes and evolution stages.

4.5. Fine-Scale Segmentation

Several lateral seismicity disruptions split the central magmatic section into subsegments and generate a stripe and gap pattern of seismic activity along the ridge. Simão et al. (2010) described a stripe and gap pattern of seismicity at the MAR as the alternation between magmatic or amagmatic spreading modes of the ridge. Their hydroacoustic data set mimics the teleseismic record of the studied ridge portion (Simão et al., 2010), which is a clear difference to our local data set. The stripe and gap pattern along the Knipovich Ridge (Figure 7) does not above all mark areas of magmatic and amagmatic spreading, but reveals a finer scaling that can be interpreted in terms of a segmentation into distinct sub-segments. When comparing our earthquake locations to the teleseismic record from the ISC catalog (only events with ISC magnitudes; Bondár & Storchak, 2011; Di Giacomo & Storchak, 2016; International Seismological Center, 2020; Storchak et al., 2017), the differences become obvious. The teleseismically recorded earthquakes (Figure S6) occur mainly south of the Logachev volcanic center. The seismicity patterns are similar south of the Logachev volcanic center, but differ directly at and north of it. The local data set is able to map small-scale variations in seismicity undetected in the teleseismic record. Curewitz et al. (2010) found that longer faults are oriented normal to plate motion, while shorter faults have various orientations indicating that higher magnitude teleseismically recorded earthquakes occur on larger fault planes imaging the general diverging plate motion. Events with smaller magnitudes occur on the smaller faults imaging more complex tectonics. These smaller events containing more details on spreading processes are missing in the teleseismic record due to the limited station coverage and uncertainties in the velocity model (Gibbons et al., 2017). Hence, we suggest that the teleseismicity and local seismicity yield two different perspectives of the same picture.

The observed stripe and gap pattern in our local data set is therefore probably caused by different processes than those observed on the teleseismic scale. The seismicity distribution to either side of the lateral disruption is different. Partly, regions with strongly contrasting seismicity characteristics are juxtaposed at short distances (km 60–80, Figure 1e), suggesting that fault zones may separate these regions. This type of

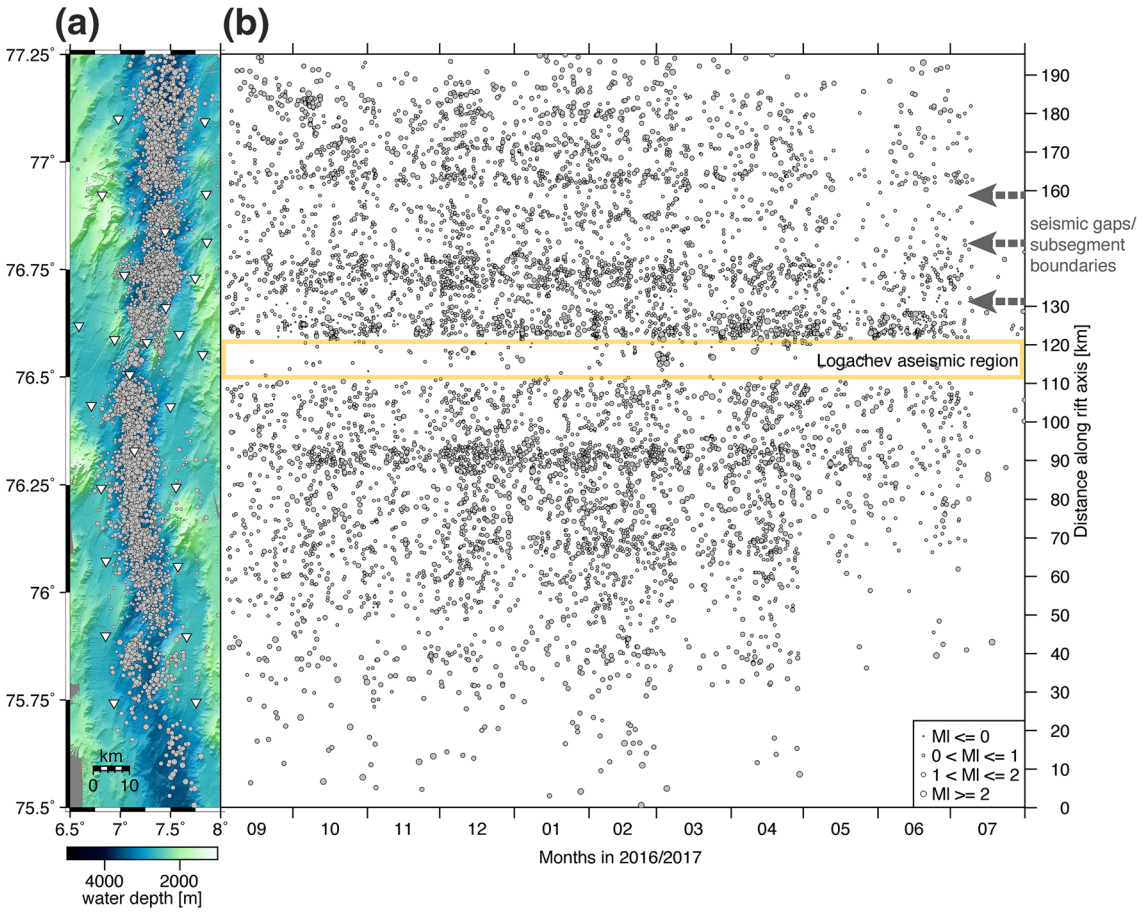

Figure 7. Stripe and gap pattern along the Knipovich Ridge in (a) map view and (b) latitude over time. Labels and symbols as in Figure 2. Yellow box marks the Logachev aseismic region, arrows mark areas of reduced seismicity (gaps) interpreted as subsegment boundaries.

fault might also prevent the migration of melt from the volcanic center as discussed before (Chapter 4.1). Since we are lacking fault plane solutions within the disruption areas, we are not able to say if small transform faults are active in the gaps allowing the reorientation of stresses and thereby juxtaposing different seismicity distributions. In addition, the unspecific, weak and depth-limited seismicity in the disruption zones differs for example from the unabated seismicity in a nontransform discontinuity west of detachment hosting segment #28 on the orthogonally spreading SWIR (Yu et al., 2018), where some strike-slip focal mechanisms could be found. We therefore speculate that on the highly oblique-spreading Knipovich Ridge, transform motion may be accommodated mostly aseismically in areas marked by the SE-NW trending lateral seismicity disruptions. Curewitz et al. (2010) showed that between en echelon highs with longer faults striking normal to the plate motion, intervening areas develop with numerous short faults oriented obliquely to the spreading direction. Potentially these short faults take up part of the oblique motion with limited seismic moment release.

5. Conclusion

From our segment-scale microseismicity study along the Knipovich Ridge, we observe characteristic patterns of seismicity leading to the following conclusions and implications on spreading modes of ultraslow spreading ridges:

- We define one predominantly magmatic segment centered around the Logachev major volcanic center, which we consider as currently active based on an aseismic region underneath the volcano and swarm

activity. The segment is defined by deepening hypocenters over 70 km in both directions along the rift axis. Melt focusing along an inferred parallel LAB can thus take place over distances of at least 70 km toward the major volcanic centers of ultraslow spreading ridges.

- This segment is further subdivided into sections with predominantly magmatic or amagmatic characteristics. The magmatic section shows shallower hypocenters, higher *b*-value and rough topography. Amagmatic sections show a distinctive lack of shallow seismicity and a deeper brittle-ductile boundary. Shallow aseismic zones may result from alteration of mantle rocks to a depth of around 9 km. Mantle rock alteration may therefore be a key process at ultraslow spreading ridges that governs deformation mechanisms. Tectonic processes like ridge reorientation may overprint the characteristics of magmatic or amagmatic sections expressed in more complex seismicity pattern.
- From our data set we cannot detect obvious detachment faults. We neither observe dipping hypocenter fault planes nor asymmetric distribution of seismicity outside clearly magmatic sections. Denser seismic networks and seismicity studies along other known detachment faults are necessary to better characterize the typical seismicity patterns associated with detachment faults.
- A finer-scale segmentation of sections is revealed by a stripe and gap pattern of enhanced and reduced seismicity. This pattern is not comparable to teleseismically detected stripe and gap patterns, with detachments producing stripes and volcanic section gaps. At the Knipovich Ridge gaps appear to mark transfer zones that possibly accommodate on small fault planes transform motion between sub-segments.

Data Availability Statement

The bathymetric raw data (dois: 10.1594/PANGAEA.895661, 10.1594/PANGAEA.895668, 10.1594/PANGAEA.892814, 10.1594/PANGAEA.892679), the seismicity raw data (Schlindwein et al., 2018, https://doi.org/10.1594/PANGAEA.896635) and earthquake catalog (Meier et al., 2020, https://doi.org/10.1594/PANGAEA.924065) are available from the Pangaea repository.

Acknowledgments
We acknowledge crew and scientists of cruises R/V Polarstern PS100 (https://doi.org/10.2312/BzPM_0705_2017, grant AWI-PS100_09), R/V Maria S. Merian MSM67 (https://doi.org/10.2312/cr_msm67) and MSM68 (https://doi.org/10.2312/cr_msm68) for their support in OBS operations. Instruments were provided by the German DEPAS pool for amphibian seismology (https://doi.org/10.17815/jlsrf-3-165) and the Polish Academy of Sciences. M. Meier received funding by the Deutsche Forschungsgemeinschaft (grant SCHL853/5-1 to V. Schlindwein). J.-R. Scholz was funded through Helmholtz Excellence Network POSY at the Alfred Wegener Institute. Participation of the Polish group was supported within statutory activities No 3841/E-41/S/2017–2020 of the Ministry of Science and Higher Education of Poland.
Open access funding enabled and organized by Projekt DEAL.

References

Albaric, J., Déverchère, J., Petit, C., Perrot, J., & Le Gall, B. (2009). Crustal rheology and depth distribution of earthquakes: Insights from the central and southern east African Rift System. *Tectonophysics*, *468*(1–4), 28–41. https://doi.org/10.1016/j.tecto.2008.05.021

Amundsen, I. M. H., Blinova, M., Hjelstuen, B. O., Mjelde, R., & Haflidason, H. (2011). The Cenozoic western Svalbard margin: Sediment geometry and sedimentary processes in an area of ultraslow oceanic spreading. *Marine Geophysical Researches*, *32*, 441–453. https://doi.org/10.1007/s11001-011-9127-z

Anderson, D. L. (1995). Lithosphere, asthenosphere, and perisphere. *Reviews of Geophysics*, *33*(1), 125–149. https://doi.org/10.1029/94RG02785

Baillard, C., Crawford, W. C., Ballu, V., Hibert, C., & Mangeney, A. (2014). An automatic kurtosis-based P- and S-phase picker designed for ocal seismic networks. *Bulletin of the Seismological Society of America*, *104*(1), 394–409. https://doi.org/10.1785/0120120347

Bohnenstiehl, D. R., Waldhauser, F., & Tolstoy, M. (2008). Frequency-magnitude distribution of microearthquakes beneath the 9°50'N region of the East Pacific Rise, October 2003 through April 2004. *Geochemistry, Geophysics, Geosystems*, *9*(10), Q10T03. https://doi.org/10.1029/2008GC002128

Bohrmann, G., Ahrlich, F., Bergenthal, M., Bünz, S., Düßmann, R., Ferreira, C., & Tao, H. (2017). R/V MARIA S. MERIAN cruise Report MSM57, gas hydrate dynamics at the continental margin of Svalbard, Reykjavik–Longyearbyen–Reykjavik, 29 July–07 September 2016. Berichte, MARUM–Zentrum für Marine Umweltwissenschaften. *Fachbereich Geowissenschaften, Universität Bremen*, *314*, 1–204.

Bondár, I., & Storchak, D. A. (2011). Improved location procedures at the international seismological center. *Geophysical Journal International*, *186*(3), 1220–1244. https://doi.org/10.1111/j.1365-246X.2011.05107.x

Bullen, K. E., & Bolt, B. A. (1985). *An introduction to the theory of seismology* (4 ed.). Cambridge: Cambridge University Press.

Burov, E. B. (2011). Rheology and strength of the lithosphere. *Marine and Petroleum Geology*, *28*(8), 1402–1443. https://doi.org/10.1016/j.marpetgeo.2011.05.008

Byerlee, J. (1978). Friction of rocks. *Pure and Applied Geophysics*, *116*, 615–626. https://doi.org/10.1007/BF00876528

Cannat, M., Fontaine, F., & Escartin, J. (2010). Serpentinization and associated hydrogen and methane fluxes at slow spreading ridges. In P. A. Rona, C. W. Devey, J. Dyment, & B. J. Murton (Eds.), Diversity of Hydrothermal Systems on Slow Spreading Ocean Ridges (Vol. 188, pp. 241–264). American Geophysical Union.

Cannat, M., Rommevaux-Jestin, C., & Fujimoto, H. (2003). Melt supply variations to a magma-poor ultra-slow spreading ridge (Southwest Indian Ridge 61° to 69°E). *Geochemistry, Geophysics, Geosystems*, *4*(8), 9104. https://doi.org/10.1029/2002GC000480

Cannat, M., Sauter, D., Bezos, A., Meyzen, C., Humler, E., & Le Rigoleur, M. (2008). Spreading rate, spreading obliquity, and melt supply at the ultraslow spreading Southwest Indian Ridge. *Geochemistry, Geophysics, Geosystems*, *9*(4). Q04002. https://doi.org/10.1029/2007GC001676

Cannat, M., Sauter, D., Lavier, L., Bickert, M., Momoh, E., & Leroy, S. (2019). On spreading modes and magma supply at slow and ultraslow mid-ocean ridges. *Earth and Planetary Science Letters*, *519*, 223–233. https://doi.org/10.1016/j.epsl.2019.05.012

Cao, A., & Gao, S. S. (2002). Temporal variation of seismic b-values beneath northeastern Japan island arc. *Geophysical Research Letters*, *29*(9), 48-1–48-3. https://doi.org/10.1029/2001GL013775

Carlson, R. L., & Miller, D. J. (2003). Mantle wedge water contents estimated from seismic velocities in partially serpentinized peridotites. *Geophysical Research Letters*, *30*(5), 1250. https://doi.org/10.1029/2002GL016600

Curewitz, D., Okino, K., Asada, M., Baranov, B., Gusev, E., & Tamaki, K. (2010). Structural analysis of fault populations along the oblique, ultra-slow spreading Knipovich Ridge, North Atlantic Ocean, 74°30′N-77°50′N. *Journal of Structural Geology*, *32*(6), 727–740. https://doi.org/10.1016/j.jsg.2009.08.011

Damm, V., & Steinborn, P., Berglar, K., Schnabel, M., Trinhammer, P., Franke, D., et al. (2017). In *Segment–Cruise No. MSM67, 31. August 2017–04. October 2017, Reykjavik (Iceland)–Longyearbyen (Svalbard)*, MARIA S. MERIAN-Berichte, (pp. 1–132). Bremen: DFG-Senatskommission für Ozeanographie. https://doi.org/10.2312/cr_msm67

deMartin, B. J., Sohn, R. A., Canales, J. P., & Humphris, S. E. (2007). Kinematics and geometry of active detachment faulting beneath the Trans-Atlantic Geotraverse (TAG) hydrothermal field on the Mid-Atlantic Ridge. *Geology*, *35*(8), 711–714. https://doi.org/10.1130/G23718A.1

DeMets, C., Gordon, R. G., & Argus, D. F. (2010). Geologically current plate motions. *Geophysical Journal International*, *181*(1), 1–80. https://doi.org/10.1111/j.1365-246X.2009.04491.x

Déverchère, J., Petit, C., Gileva, N., Radziminovitch, N., Melnikova, V., & San'kov, V. (2001). Depth distribution of earthquakes in the Baikal rift system and its implications for the rheology of the lithosphere. *Geophysical Journal International*, *146*(3), 714–730. https://doi.org/10.1046/j.0956-540x.2001.1484.484.x

Di Giacomo, D., & Storchak, D. A. (2016). A scheme to set preferred magnitudes in the ISC Bulletin. *Journal of Seismology*, *20*, 555–567. https://doi.org/10.1007/s10950-015-9543-7

Ekström, G., Nettles, M., & Dziewoński, A. M. (2012). The global CMT project 2004-2010: Centroid-moment tensors for 13,017 earthquakes. *Physics of the Earth and Planetary Interiors*, *200–201*, 1–9. https://doi.org/10.1016/j.pepi.2012.04.002

Elkins, L. J., Sims, K. W. W., Prytulak, J., Blichert-Toft, J., Elliott, T., Blusztajn, J., & Schilling, J.-G. (2014). Melt generation beneath Arctic Ridges: Implications from U decay series disequilibria in the Mohns, Knipovich, and Gakkel Ridges. *Geochimica et Cosmochimica Acta*, *127*, 140–170. https://doi.org/10.1016/j.gca.2013.11.031

Escartin, J., Hirth, G., & Evans, B. (1997). Effects of serpentinization on the lithospheric strength and the style of normal faulting at slow-spreading ridges. *Earth and Planetary Science Letters*, *151*(3–4), 181–189. https://doi.org/10.1016/S0012-821X(97)81847-X

Escartin, J., Hirth, G., & Evans, B. (2001). Strength of slightly serpentinized peridotites: Implications for the tectonics of oceanic lithosphere. *Geology*, *29*(11), 1023–1026. https://doi.org/10.1130/0091-7613(2001)029<1023:SOSSPI>2.0.CO;2

Escartin, J., Smith, D. K., Cann, J., Shouten, H., Langmuir, C. H., & Escrig, S. (2008). Central role of detachment faults in accretion of slow-spreading oceanic lithosphere. *Nature*, *455*, 790–794. https://doi.org/10.1038/nature07333

Gibbons, S. J., Harris, D. B., Dahl-Jensen, T., Kværna, T., Larsen, T. B., Paulsen, B., & Voss, P. H. (2017). Locating seismicity on the Arctic plate boundary using multiple-event techniques and empirical signal processing. *Geophysical Journal International*, *211*(3), 1613–1627. https://doi.org/10.1093/gji/ggx398

Grevemeyer, I., Reston, T. J., & Moeller, S. (2013). Microseismicity of the Mid-Atlantic Ridge at 7°S–8°15′S and at the Logatchev Massif oceanic core complex at 14°40′N–14°50′N. *Geochemistry, Geophysics, Geosystems*, *14*(9), 3532–3554. https://doi.org/10.1002/ggge.20197

Gutenberg, B., & Richter, C. F. (1944). Frequency of earthquakes in California. *Bulletin of the Seismological Society of America*, *34*(4), 185–188.

Hannemann, K., Krüger, F., & Dahm, T. (2014). Measuring of clock drift rates and static time offsets of ocean bottom stations by means of ambient noise. *Geophysical Journal International*, *196*(2), 1034–1042. https://doi.org/10.1093/gji/ggt434

Havskov, J., & Ottemöller, L. (1999). SeisAN Earthquake analysis software. *Seismological Research Letters*, *70*(5), 532–534. https://doi.org/10.1785/gssrl.70.5.532

Heimann, S., Kriegerowski, M., Isken, M., Cesca, S., Daout, S., Grigoli, F., et al. (2017). *Pyrocko–An open-source seismology toolbox and library. V 0.3*. GFZ Data Services. https://doi.org/10.5880/GFZ.2.1.2017.001

Hellevang, B., & Pedersen, R. B. (2005). Magmatic segmentation of the northern Knipovich Ridge: Evidence for high-pressure fractionation at an ultraslow spreading ridge. *Geochemistry, Geophysics, Geosystems*, *6*(9), Q09007. https://doi.org/10.1029/2004GC000898

Horning, G., Sohn, R. A., Canales, J. P., & Dunn, R. A. (2018). Local seismicity of the rainbow massif on the Mid-Atlantic Ridge. *Journal of Geophysical Research: Solid Earth*, *123*(2), 1615–1630. https://doi.org/10.1002/2017JB015288

International Seismological Centre (2020). *On-line bulletin*. International Seismological Centre. https://doi.org/10.31905/D808B830

Jokat, W., Kollofrath, J., Geissler, W. H., & Jensen, L. (2012). Crustal thickness and earthquake distribution south of the Logachev Seamount, Knipovich Ridge. *Geophysical Research Letters*, *39*(8), L08302. https://doi.org/10.1029/2012GL051199

Kanzow, T. (2017). The expedition PS100 of the research vessel POLARSTERN to the fram strait in 2016. *Reports on Polar and Marine Research*, *705*. 175. https://doi.org/10.2312/BzPM_0705_2017

Kissling, E. (1995). *Program VELEST USER'S GUIDE–short introduction*. Switzerland. Institute of Geophysics, ETH Zurich.

Kokhan, A. V., Dubinin, E. P., Grokholsky, A. L., & Abramova, A. S. (2012). Kinematics and characteristic features of the morphostructural segmentation of the Knipovich Ridge. *Oceanology*, *52*(5), 688–699. https://doi.org/10.1134/S0001437012050098

Kvarven, T., Hjelstuen, B. O., & Mjelde, R. (2014). Tectonic and sedimentary processes along the ultraslow Knipovich spreading ridge. *Marine Geophysical Researches*, *35*, 89–103. https://doi.org/10.1007/s11001-014-9212-1

Lehnert, K., Su, Y., Langmuir, C., Sarbas, B., & Nohl, U. (2000). A global geochemical database structure for rocks. *Geochemistry, Geophysics, Geosystems*, *1*(5), 1012. https://doi.org/10.1029/1999GC000026

Libak, A., Eide, C. H., Mjelde, R., Keers, H., & Flüh, E. R. (2012). From pull-apart basins to ultraslow spreading: Results from the western Barents Sea Margin. *Tectonophysics*, *514–517*, 44–61. https://doi.org/10.1016/j.tecto.2011.09.020

Lomax, A., Virieux, J., Volant, P., & Berge-Thierry, C. (2000). *Probabilistic earthquake location in 3D and layered models*. In C. H. Thurber, & N. Rabinowitz (Eds.), Advances in Seismic Event Location. Modern Approaches in Geophysics (Vol. *18*). Dordrecht: Springer. https://doi.org/10.1007/978-94-015-9536-0_5

McKenzie, D., Jackson, J., & Priestly, K. (2005). Thermal structure of oceanic and continental lithosphere. *Earth and Planetary Science Letters*, *233*(3–4), 337–349. https://doi.org/10.1016/j.epsl.2005.02.005

Meier, M., & Schlindwein, V. (2018). First in situ seismic record of spreading events at the ultraslow spreading southwest Indian Ridge. *Geophysical Research Letters*, *45*(19), 10360–10368. https://doi.org/10.1029/2018GL079928

Meier, M., Schlindwein, V., & Scholz, J. R. (2020). *Microearthquake catalogue at the Knipovich Ridge 75.5-77.5N from 2016-09 till 2017-07*. PANGAEA. https://doi.org/10.1594/PANGAEA.924065

Mével, C. (2003). Serpentinization of abyssal peridotites at mid-ocean ridges. *Comptes Rendus Geoscience*, *335*(10–11), 825–852. https://doi.org/10.1016/j.crte.2003.08.006

Michael, P. J., Langmuir, C. H., Dick, H. J. B., Snow, J. E., Goldstein, S. L., Graham, D. W., & Edmonds, H. N. (2003). Magmatic and Amagmatic seafloor generation at the ultraslow-spreading Gakkel Ridge, Arctic Ocean. *Nature*, *423*(6943), 956–961. https://doi.org/10.1038/nature01704

Momoh, E., Cannat, M., Watremez, L., Leroy, S., & Singh, S. C. (2017). Quasi-3-D seismic reflection imaging and wide-angle velocity structure of nearly Amagmatic oceanic ithosphere at the ultraslow-spreading southwest Indian Ridge. *Journal of Geophysical Research: Solid Earth*, *122*(12), 9511–9533. https://doi.org/10.1002/2017JB014754

Montési, L. G. J., Behn, M. D., Hebert, L. B., Lin, J., & Barry, J. L. (2011). Controls on melt migration and extraction at the ultraslowSouthwest Indian Ridge 10°–16°E. *Journal of Geophysical Research*, *116*. B10102. https://doi.org/10.1029/2011JB008259

Okino, K., Curewitz, D., Asada, M., Tamaki, K., Vogt, P., & Crane, K. (2002). Preliminary analysis of the Knipovich Ridge segmentation: Influence of focused magmatism and ridge obliquity on an ultraslow spreading system. *Earth and Planetary Science Letters*, *202*(2), 275–288. https://doi.org/10.1016/S0012-821X(02)00790-2

Ottemöller, L., Voss, P., & Havskov, J. (2017). *SEISAN earthquake analysis software for windows, solaris, linux and macosx.*

Parnell-Turner, R., Sohn, R. A., Peirce, C., Reston, T. J., MacLeod, C. J., Searle, R. C., & Simão, N. M. (2017). Oceanic detachment faults generate compression in extension. *Geology*, *45*(10), 923–926. https://doi.org/10.1130/G39232.1

Ranalli, G. (1995). *Rheology of the Earth* (2nd edn.). Netherlands: Springer.

Reston, T. J., & McDermott, K. G. (2011). Successive detachment faults and mantle unroofing at magma-poor rifted margins. *Geology*, *39*(11), 1071–1074. https://doi.org/10.1130/G32428.1

Sauter, D., & Cannat, M. (2010). *The ultraslow spreading Southwest Indian Ridge*. In P. A. Rona, C. W. Devey, J. Dyment, & B. J. Murton (Eds.), Diversity of Hydrothermal Systems on Slow Spreading Ocean Ridges (Vol. *188* pp. 153–173), American Geophysical Union. https://doi.org/10.1029/2008GM000843

Sauter, D., Cannat, M., Rouméjon, S., Andreani, M., Birot, D., Bronner, A., & Searle, R. (2013). Continuous exhumation of mantle-derived rocks at the southwest Indian Ridge for 11 million years. *Nature Geoscience*, *6*, 314–320. https://doi.org/10.1038/NGEO1771

Sauter, D., Patriat, P., Rommevaux-Jestin, C., Cannat, M., Briais, A., & Gallieni (2001). Shipboard Scientific Party.The Southwest Indian Ridge between 49°15′E and 57°E: Focused accretion and magma redistribution. *Earth and Planetary Science Letters*, *192*(3), 303–317. https://doi.org/10.1016/S0012-821X(01)00455-1

Schlindwein, V., Demuth, A., Geissler, W. H., & Jokat, W. (2013). Seismic gap beneath Logachev Seamount: Indicator for melt focusing at an ultraslow mid-ocean ridge?. *Geophysical Research Letters*, *40*(9), 1703–1707. https://doi.org/10.1002/grl.50329

Schlindwein, V., Demuth, A., Korger, E., Läderach, C., & Schmid, F. (2015). Seismicity of the Arctic mid-ocean Ridge system. *Polar Science*, *9*(1), 146–157. https://doi.org/10.1016/j.polar.2014.10.001

Schlindwein, V., Krüger, F., Schmid, F., Schmidt-Aursch, M., Brune, R., Dorgerloh, F., et al. (2017). In *KNIPAS–Knipovich Ridge Passive Seismic Experiment, Cruise No. MSM68, October 6–October 18, 2017, Svalbard (Norway)–Emden (Germany)*, MARIA S. MERIAN-Berichte (pp. 1–53). Bremen: DFG-Senatskommission für Ozeanographie. https://doi.org/10.2312/cr_msm68

Schlindwein, V., Krüger, F., & Schmidt-Aursch, M. (2018). *Project KNIPAS: DEPAS ocean-bottom seismometer operations in the Greenland sea in 2016-2017*. Bremerhaven, PANGAEA: Alfred Wegener Institute, Helmholtz Centre for Polar and Marine Research. https://doi.org/10.1594/PANGAEA.896635

Schlindwein, V., & Schmid, F. (2016). Mid-ocean-ridge seismicity reveals extreme types of ocean lithosphere. *Nature*, *535*, 276–279. https://doi.org/10.1038/nature18277

Schmid, F., & Schlindwein, V. (2016). Microearthquake activity, lithospheric structure, and deformation modes at an amagmatic ultraslow spreading Southwest Indian Ridge segment. *Geochemistry, Geophysics, Geosystems*, *17*(7), 2905–2921. https://doi.org/10.1002/2016GC006271

Schmid, F., Schlindwein, V., Koulakov, I., Plötz, A., & Scholz, J.-R. (2017). Magma plumbing system and seismicity of an active mid-ocean ridge volcano. *Scientific Reports*, *7*, 42949. https://doi.org/10.1038/srep42949

Schmidt-Aursch, M., & Haberland, C. (2017). DEPAS (Deutscher Geräte-Pool für amphibische Seismologie): German instrument pool for amphibian seismology. *Journal of Largescale Research Facilities*, *3*, A122. https://doi.org/10.17815/jlsrf-3-165

Scholz, C. H. (2002). *The mechanics of earthquakes and faulting* (2nd ed.). Cambridge: Cambridge University Press. https://doi.org/10.1017/9781316681473.

Schweitzer, J. (2001). HYPOSAT–An enhanced routine to locate seismic events. *Pure and Applied Geophysics*, *158*, 277–289. https://doi.org/10.1007/PL00001160

Schweitzer, J. (2018). *User manual HYPOSAT 6 and HYPOMOD 2*.

Simão, N., Escartin, J., Goslin, J., Haxel, J., Cannat, M., & Dziak, R. (2010). Regional seismicity of the Mid-Atlantic Ridge: Observations from autonomous hydrophone arrays. *Geophysical Journal International*, *183*(3), 1559–1578. https://doi.org/10.1111/j.1365-246X.2010.04815.x

Smith, D. K., Escartin, J., Cannat, M., Tolstoy, M., Fox, C. G., Bohnenstiehl, D. R., & Bazin, S. (2003). Spatial and temporal distribution of seismicity along the northern Mid-Atlantic Ridge (15°–35°N). *Journal of Geophysical Research*, *108*(B3), 2167. https://doi.org/10.1029/2002JB001964

Snoke, J. A., Munsey, J. W., Teague, A. G., & Bollinger, G. A. (1984). A program for focal mechanism determination by combined use of polarity and SV-P amplitude ratio data. *Earthquake Notes*, *55*, 15.

Stähler, S. C., Schmidt-Aursch, M. C., Hein, G., & Mars, R. (2018). A self-noise model for the German DEPAS OBS Pool. *Seismological Research Letters*, *89*(5), 1838–1845. https://doi.org/10.1785/0220180056

Standish, J. J., Dick, H. J. B., Michael, P. J., Melson, W. G., & O'Hearn, T. (2008). MORB generation beneath the ultraslow spreading southwest Indian Ridge (9–25°E): Major element chemistry and the importance of process versus source. *Geochemistry, Geophysics, Geosystems*, *9*(5), Q05004. https://doi.org/10.1029/2008GC001959

Storchak, D. A., Harris, J., Brown, L., Lieser, K., Shumba, B., Verney, R., & Korger, E. I. M. (2017). Rebuild of the bulletin of the international seismological centre (ISC), part 1: 1964–1979. *Geoscience Letters*, *4*, 32. https://doi.org/10.1186/s40562-017-0098-z

Tao, C., Seyfried, W. E., Jr, Lowell, R. P., Liu, Y., Liang, J., Guo, Z., & Li, W. (2020). Deep high-temperature hydrothermal circulation in a detachment faulting system on the ultra-slow spreading ridge. *Nature Communications*, *11*, 1300. https://doi.org/10.1038/s41467-020-15062-w

Tolstoy, M., Bohnenstiehl, D. R., Edwards, M. H., & Kurras, G. J. (2001). Seismic character of volcanic activity at the ultraslow-spreading Gakkel Ridge. *Geology*, *29*(12), 1139–1142. https://doi.org/10.1130/0091-7613(2001)029<1139:SCOVAA>2.0.CO;2

Wiemer, S., & Wyss, M. (2000). Minimum magnitude of complete reporting in earthquake catalogs: Examples from Alaska, the Western United States, and Japan. *Bulletin of the Seismological Society of America*, *90*(4), 859–869. https://doi.org/10.1785/0119990114

Woessner, J., & Wiemer, S. (2005). Assessing the quality of earthquake catalogues: Estimating the magnitude of completeness and its uncertainty. *Bulletin of the Seismological Society of America*, *95*(2), 684–698. https://doi.org/10.1785/0120040007

Wyss, M., Hasegawa, A., Wiemer, S., & Umino, N. (1999). Quantitative mapping of precursory seismic quiescence before the 1989, M 7.1 off-Sanriku earthquake, Japan. *Annals of Geophysics*, *42*(5), 851–869. https://doi.org/10.4401/ag-3765

Yu, Z., Li, J., Niu, X., Rawlinson, N., Ruan, A., Wang, W., & Liang, Y. (2018). Lithospheric structure and tectonic processes constrained by microearthquake activity at the central ultraslow-spreading southwest Indian Ridge (49.2° to 50.8°E). *Journal of Geophysical Research: Solid Earth*, *123*(8), 6247–6262. https://doi.org/10.1029/2017JB015367

Zarayskaya, Y. A. (2017). Segmentation and seismicity of the ultraslow Knipovich and Gakkel Mid-Ocean Ridges. *Geotectonics*, *51*(2), 163–175. https://doi.org/10.1134/S0016852117010095